Flow stability and regime transitions on periodic open foams

Yann Jobic, Marc Médale, Frédéric Topin

Flow stability and regime transitions on periodic open foams

Yann Jobic[1*], Marc Médale[1] and Frédéric Topin[1]

[1*]Aix-Marseille Université, CNRS, IUSTI UMR 7343, 5 rue E. Fermi, Marseille, 13453, France.

*Corresponding author(s). E-mail(s): yann.jobic@univ-amu.fr;
Contributing authors: marc.medale@univ-amu.fr;
frederic.topin@univ-amu.fr;

Abstract

This study aims to link critical Reynolds numbers associated with either steady-state or temporal bifurcations to fluid flow regimes described by macroscopic laws (Darcy, Forchheimer) in a periodic 3D Kelvin foam, using direct numerical simulations. We first identify the permeability and inertial coefficient of the Darcy's law and the Forchheimer's one. We explicit the different flow regimes that are accounted for in the Forchheimer's framework (Darcian, weak inertia and strong inertia regimes, respectively). We present an original systematic way to determine the critical Reynolds number associated with both regime transitions. We calculate them over a wide range of porosities and present two power-law correlations that locate these regime transitions for engineering purposes.

We have performed pore-scale resolved calculations for various porosities with the Asymptotic Numerical Method (ANM) to find steady-state bifurcations, if any, along with a Linear Stability Analysis (LSA) to find temporal (Hopf) bifurcations from steady-state base flows. All the computed bifurcations occur at Reynolds numbers in the vicinity of the transition from weak to strong inertia regimes, where a change of behavior takes place. On the other hand, no bifurcation has been found in the transition between Darcian and weak inertia regimes.

Keywords: Incompressible Navier-Stokes equations, Darcy's law, Forchheimer's law, Asymptotic Numerical Method, Linear Stability Analysis, Steady-state and Hopf bifurcations

1 Introduction

Predicting flow structures in porous media is a key task in several environmental and industrial applications (hydro-geology, geothermal energy, chemical engineering, etc., to quote a few). This rich field has been widely studied for the last two centuries. The pioneering approach is due to Darcy [1], who identified a macroscopic law for creeping flows in a packed-sand beds. Specific macroscopic properties associated with the porous media were at that time only determined from experiments. It has been verified countless times and it linearly relates the macroscopic gradient of the fluid phase average pressure $\partial < p_f > /\partial x$ ($\mathrm{Pa.m^{-1}}$) to the filtration (or Darcian, superficial) velocity u ($\mathrm{m.s^{-1}}$), as follows:

$$-\frac{\partial < p >^f}{\partial x} = \mu K_D^{-1} u, \tag{1}$$

with μ the dynamic viscosity of the fluid (Pa.s) and K_D the permeability ($\mathrm{m^2}$) of the porous media.

Also from experimental observations, Forchheimer ([2]) extended the Darcy's law to accommodate a wider range of velocities by adding a quadratic term into Eq. 1, which accounts for the fluid-flow kinetic energy. So, the Forchheimer's law reads:

$$-\frac{\partial < p >^f}{\partial x} = au + bu^m, \tag{2}$$

where a is a constant related to the first order polynomial in u, b is the inertia coefficient, that depends on the geometry of the porous media (e.g., strut shape, tortuosity, etc.), and the power coefficient m is close to 2. We have written eq. 2 in a general way to describe the different methods used for the identification of macroscopic parameters (a,b) that enter the law. They are related to the way one determines a and b by fitting experimental or from computations at pore-scale data-points. The uniqueness of the solution is not guaranteed and strongly depends on the working range of Reynolds numbers ([3]).

There are three main ways to determine (a,b). The first one is to identify a from the permeability defined from the Darcy's equation, eq. 1. In a second step, one looks for b, keeping a fixed ([4, 5]). This method is mainly used with numerical simulations, as it's very difficult to obtain accurate experimental data in the Darcian regime ([5])for such media. A second method determines b first as one intends to fit the high inertia regime (high Reynolds numbers). Then, a is determined with b fixed. Finally, the third, mostly used, method is to determine (a,b) altogether, by fitting directly the curve of the pressure drop as a function of the filtration velocity. The differences between those methods can be found in [6], which shows a difference of 20-97% for the permeability, and up to 6% for the inertia coefficient. In other words, this method while often used for engineering applications leads to coefficient values valid only for the range of identification and may leads to significant errors in the prediction of pressure drop outside of this range (e.g. for creeping flow conditions that are often extrapolated in industrial situations)

However, as the macroscopic flow law strongly depends on the flow regime, there is a need to correctly characterize the validity domain of the previous macroscopic laws, together with transition regions between them. Three zones are usually identified in the related literature [7, 8]. The first one is called the Darcian zone, where viscous effect are dominant with respect to inertia terms, and corresponds at the pore scale to a Stokes flow. In this region, the Darcy's law is valid and accurate and predicts that the filtration velocity linearly depends on the macroscopic pressure drop.
The third zone corresponds to the range of high Reynolds numbers, where turbulence occurs, characterized by unsteady and chaotic flows. In this zone, non-linear effects are dominant.
The second zone is the transition zone in between the two previous ones. The inertia effects are of the same order of magnitude than the viscous ones. It is well established [9, 10] that we can divide this zone in two secondary sub-zones. The first one defines the limit from Darcy to what we call *the weak inertia regime*. In this sub-zone, the higher the filtration velocity, the greater the pressure drop deviates from the Darcy law (eq. 1). There is therefore a transition between the Darcy zone and the weak inertia one. Moreover, as the Reynolds number increases, the non-linear effects become dominant, while the flow remains laminar at the pore scale. We call this zone the *strong inertia regime*, which is different from turbulent flows. There is also a transition from weak inertia to strong inertia regimes or zones, to be defined. All those transitions may be related to the Reynolds number ($Re = \frac{\rho u L}{\mu}$), which obviously depends on the choice of the reference length-scale L. Note that the Forchheimer equation models at the macroscopic scale all of those zones with a reasonable accuracy.

Aside the two famous macroscopic laws (Darcy and Forchheimer equations), some other works have been devoted to recover macroscopic laws from theoretical developments. Different techniques were used, e.g., from dimensional analysis [11], capillary models [12], averaging methods [13], asymptotic expansions [14], volume averaging [15], etc. Those developments were correlated to the need to understand the physical meaning of the above macroscopic laws.
However, the origin of the deviation from Darcy's law is not yet completely understood. Indeed, it was first attributed to turbulence ([8], p.62), even for low Reynolds numbers (of values ranging from 1 to 10 in that reference). However, as the flow exhibits non-linear effects without turbulence at even lower Reynolds numbers, other explanations should be advanced. Giorgi ([14]) suggested that it could originate from the inertial microscopic forces and lead to a dependence of the inertia coefficient to the filtration velocity of the Forchheimer's law.

The increase of computational power enables nowadays to compute the Navier-Stokes equations at pore scale in realistic 3D geometries. Indeed, they quantitatively describe the fluid flow behavior for all Reynolds numbers, provided one assigns suitable spatial resolution to the considered hydrodynamic regime. Moreover, CFD computations at pore scale give access to a large amount of information, such as streamlines, fluid accelerations, flow variation around the mean one, drag forces, etc. So, by upscaling the computed flow fields, one can identify the macroscopic parameters.

Various numerical methods have been used: Finite Element Method ([16]), Lattice Boltzmann Method [17, 18], along with commercial softwares ([4, 19]), etc. The main idea is to find laws describing the dependency of the macroscopic properties of the porous media to intrinsic geometric parameters (such as porosity, tortuosity, etc.). We can cite the famous Ergun's law ([20], which links the pressure drop to the porosity and the grain size. This work leads to many variations (experimental and numerical ones) depending of the corresponding field (a review can be found in [16], table 2). Moreover this formulation developed for packed bed of spheres has been applied to many other media and it has been shown that the macroscopic flow laws depends also on other geometric quantities.

The bridge between computations at the pore scale and macroscopic laws is the existence of elementary representative volume from some periodic geometry that could be found in the porous media. Among idealized elementary representative volumes is the Kelvin cell, for which a comprehensive survey of macroscopic flow laws is presented in [21]. Among all the pressure drop studies and correlations presented in this review paper, critical remarks are summarized as the follows:

- The permeability and inertia coefficients are very sensitive to the porosity range (mainly low-porosity range) and are strictly strut shape dependent;
- Separate determination of flow law characteristics (K_D and C_{For} in viscous and inertia regimes) is needed. Extraction of permeability from second-order polynomial pressure drop data would lead to wrong values of Darcian permeability in the viscous regime;
- Values of Ergun's parameters vary clearly with porosity and strut shape and do not possess constant numerical values;
- Common definition of characteristic length scale (and associated measurements) is missing to reduce the dispersion in friction factor data.

Thermal instabilities in foams are first studied at the macroscopic level, using Darcy's laws for the flow (see for example [22–24]). Those studies aim to examine the convective heat transfer in a homogeneous porous duct of rectangular cross section. They link the stability to the Rayleigh number, and find for those configurations some Hopf bifurcations. Another classical approach, also at macroscopic level, is to study the stability of the flow overlaying a porous layer, also modeled at the macroscopic level (see for e.g. [25–27]). They are interested in the interaction between the flow and the porous layer, in term of production or dissipation of kinetic energy, linking it to instabilities.
However, the study of fluid-flow instabilities at pore level in 3D foam is a new topic. To our knowledge, only one paper reported 2D bifurcations into periodic ordered and disordered non-deformable porous structures, composed of squares or circles ([28]). For each porous medium, a systematic study of increasing mass-flow rate was performed for unsteady Navier-Stokes equations, giving the critical Reynolds numbers of the Hopf bifurcations. Instabilities of 2D fluidic pinball has also been studies [29]. We can note that 3D flow and/or instabilities have no reason to be identical to 2D ones.

For example, critical Reynolds number of the Hopf bifurcation for the flow over a 2D circular cylinder arise at about Re_c=43, for the 3D cylinder Re_c=188, and for the 3D sphere, Re_c=277. Therefore, critical Reynolds number of the same shape family leads to very different values in 2D and 3D. In the present work we are interested in intrinsic 3D geometries, presenting their own complexities.

So, to address some of the above remarks, the present work aims to compute the incompressible Navier-Stokes equations at pore level in a Kelvin's like foam to provide reference values for the identification of macroscopic laws. Moreover, we also have computed the instabilities that take place and identified critical Reynolds numbers at which they occur. Indeed, we have computed both steady-state and Hopf bifurcations, depending on the fluid-flow regime. The outcome of this work is to relate the computed instabilities to the transitions in macroscopic flow regime predicted by macroscopic laws or correlations.

2 Numerical methods

We are interested in the study of real foams, however, they are too complex as we can not control individually each parameters (e.g., strut shape, pore elongation, different local porosities, etc). Moreover, the individual manufacturing process of each producer (even each batch) lead to specific relations between the geometrical parameters of the commercially available samples. Therefore, the Kelvin foam structure, a widely recognized idealized structure of real foams, has been chosen. Its symmetries enable to restrict the computational domain to the periodic pattern and thus strongly reduce computational cost. The chosen strut shape is triangular, with various cross-section to change the porosity. The present study is deliberately focused on the high porosity range ($68\% < \varepsilon < 97\%$), which is of industrial application relevance.

At pore scale, we consider an incompressible fluid-flow in laminar regime, which is governed by the Incompressible Navier-Stokes equations:

$$\begin{aligned} \frac{\partial \mathbf{v}}{\partial t} + (\mathbf{v} \cdot \nabla)\mathbf{v} &= -\nabla p + \frac{1}{\mathrm{Re}} \nabla^2 \mathbf{v}, \\ \nabla \cdot \mathbf{v} &= 0, \end{aligned} \tag{3}$$

with $\mathbf{v}$ the velocity vector at the $\mathbf{x}$ position, p is the pressure, Re is the Reynolds number based on the relevant length-scale L ($Re = \rho U L/\mu$) and t is time.

Periodical boundary conditions are imposed along the streamwise direction (Z direction), meanwhile symmetry conditions are applied along the span-wise horizontal directions (X and Y directions). The periodic condition is implemented by changing the connectivity of the elements While the symmetry conditions are obtained by cancelling the transverse gradient on the appropriate surfaces As we consider the streamwise periodicity of the flow, the fluid flow is driven by a macroscopic body force along the Z direction.

The governing equations are discretized in space by the Galerkin Finite Element Method [30, 31], with tri-quadratic Lagrange polynomial approximations for the velocity and a linear one for the pressure to satisfy the Ladyzhenskaya–Babuška–Brezzi (LBB) condition.
Three complementary algorithms have been used in the present work:

- a steady-state continuation algorithm, based on the Asymptotic Numerical Method (ANM, [32, 33]) to compute the branches of steady-state solutions;
- a Linear Stability Analysis algorithm to compute the generalized eigenvalue problem associated with the linear stability of steady-state solutions ([34, 35]);
- a time integration algorithm of the Incompressible Navier-Stokes equations, based on an unconditionally stable projection method ([36]) to compute unsteady fluid flows.

When looking for a steady solution, when it exists, we have used a penalized formulation of the governing equations which enables direct access to the solution. However, at high Reynolds numbers this process leads to solve a highly non-linear problem. Therefore, one uses the ANM to compute this non-linear solution with a continuation algorithm([37]). Moreover this continuation algorithm computes the various branches of steady-state solutions if present, i.e. when it exists steady-state bifurcations. The ANM is based on the combination of a perturbation method and a continuation one. The perturbation method introduces high-order Taylor series representation of the unknowns along with the continuation parameter. So, it transforms a highly non-linear and implicit parametric problem into a series of linear ones. As a continuation algorithm, it is based on the implicit function theorem that enables to extrapolate a regular (continuous and derivable) initial solution to its vicinity along the loading parameter for a regular solution. It is therefore a high-order predictor/corrector algorithm in which the correction stage is performed with a Newton-Raphson algorithm, if needed.

To overcome the very poor conditioning of the penalized formulation, the resulting algebraic systems are solved with the direct parallel MUMPS (LU parallel) solver ([38, 39]). This formulation can significantly reduce the computational cost of steady-state problems, compared to any time-marching algorithm. On the other hand, this method is costly in terms of RAM, especially for 3D computations.

The implementation of the steady-state solver with the ANM continuation algorithm is performed into the massively parallel PETSc framework library ([40–42]).

The ANM algorithm enables to compute all steady-state solutions (stable and unstable ones), but also to detect and compute steady-state bifurcations, if any. Therefore it has to be complemented by a Linear Stability Analysis (LSA) in order to find out other bifuraction types, such as Hopf bifurcations.

In the present work, the LSA of steady-state solutions relies on the normal mode analysis. This method consists in the linearization of the Navier-Stokes equations by applying a perturbation of exponential form in time. The solution can this way be decomposed into normal modes. The stability analysis of the steady-state solution is achieved by solving a generalized eigenvalue problem owing to the Finite Element discretization of the dynamical terms (the mass matrix). We apply this method to each steady-state solution computed by the ANM. The implementation of this linear

analysis aglorithm is performed with the SLEPc library ([43]), which relies on the PETSc one.

For the unsteady calculations, the use of a projection algorithm leads to a "segregated" approach, which consists in successively compute velocity-pressure sub-problems. This choice has two main consequences from a numerical and computational point of view. The first consequence is that the size of each sub-system is reduced, and more importantly that the conditioning of each algebraic sub-system is significantly improved compared to the original global problem. This allows us to efficiently solve these systems with iterative methods (of preconditioned Krylov subspace type), and this on massively parallel architectures. Regarding the solution of the incompressible Navier-Stokes equations, we have implemented the inconditionnaly stable algorithm of Guermond-Shen ([36]). The time integration is performed with a first order Backward Euler scheme with appropriate time steps.

3 Results and discussion

The quality of the numerical solution depends strongly on the quality of the mesh, specially for the presented numerical tools. Indeed, the ANM relies on high order power series in a recursive way. The numerical errors could then adds up in a dramatic way. We then want hexahedral meshes as it's the one that offers accurate solutions compared to others (tetrahedral, pyramids, ...), provided they are not too much distorted (invertible geometric transformation from parametric to actual elements). However, the mesh should correctly describe the geometry (negligible geometric discretization errors). Note this structure is an idealized Kelvin Cell (see Fig. 1) as it is composed of straight struts of nearly equilateral triangle cross-section (often named Kelvin Like Cell) while the original Kelvin Cell is composed of sligthly curved struts as it is the dual of stacked interpenetrating spheres. Gyroid surfaces are also used to create Kelvin cell structure.

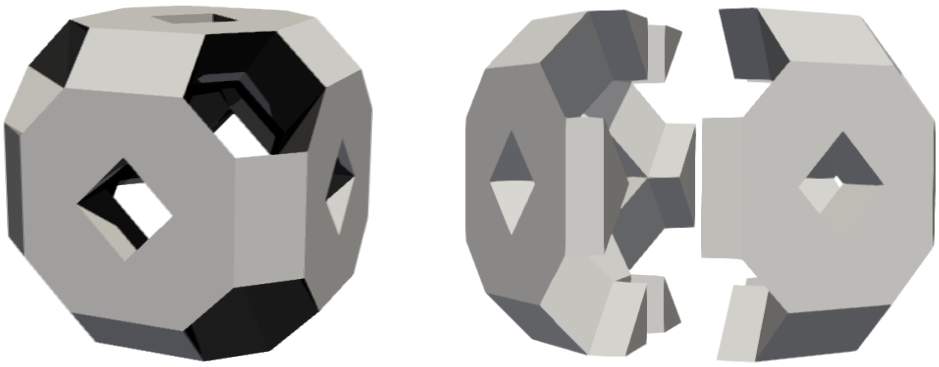

(a) A Kelvin cell.

(b) Exploded view of the same cell.

Fig. 1: Solid phase of a Kelvin cell with triangular struts (porosity $\varepsilon = 68.3\%$).

There are many ways to create these geometric structures. The basic idea is to start with a truncated octahedron. Then a first option is to create strut cross section centered along the edge of the face and extrude them; this method is simple, fast as there is many symmetry planes, allow to parametrically create various strut shape and cross section and associated unstructured meshes [44]. On the other hand, the subdivision of the poral space (usually obtained via boolean subtraction of the assembled struts from a bounding cube) in hexahedral patches if needed is tedious and complicated. We thus choose to construct directly the poral space.
The domain was obtained by extruding (outward, normal) several faces of the truncated octahedron and taking advantage of the symmetries. The resulting structure is the poral space of a triangular strut Kelvin cell formed by the empty spaces left by the extrusion process [45]. This space is then easily subdivided in hexahedral shapes that are paved with structured hex meshes. The resulting mesh is isotropic and periodic with only high-quality hexahedral elements, as presented Fig. 2.
This conformal mesh possesses a complicated periodicity, consisting in one cell plus two half-cells in two directions, and one in the last one. It's however periodic in all the directions. We can generate different porosities by changing the extrude length (which correspond to the strut cross section edge length), which also change the size of the Kelvin cell. The inner volume of the cell (the original truncated octahedron) stay the same, but the distance between struts centerline change and thus also the size of the bounding cuboid enclosing the Kelvin cell.

This domain discretization quality is of primary importance for numerical precision at higher Reynolds numbers, as the inertia term comes into play.
A previous attempt has been made to use a regular structured grid generated by a marching cube algorithm applied to the Kelvin cell. In this case, the unstructured mesh is perfect in the numerical way (small cubes), but it is aligned with the Cartesian coordinate system and does not follow correctly the geometry, creating a staircase effect on the struts-fluid interfaces. Refining the mesh creates different porous media (the geometrical discretisation errors change with the mesh size), with different properties (mostly porosity, specific surface area, and the interface roughness that is artificially added). Considering these bias we prefer a initially more complicated but far more efficient mesh creation procedure to ensure that mesh convergence studies were carried out on the exact same geometry. Note : The dependency of the permeability (D_{bc}^2), inertia coefficient (D_{bc}^{-1}) as well as the geometrical parameters of the Kelvin cell with the size of the Kelvin cell (here the dimension of the bounding cube - D_{bc} -) is well known and could be removed from all further analysis [46].
Figure 3 depict the results of a pore scale simulation at $\mathrm{Re}_{Dh} = 183.7$, using the hydraulic diameter Dh as the length scale (see below). We can observe the complicated flow path going around the struts,with the streamlines highlighting some recirculation patterns. That dynamic is complex, and is difficult to extract simple -scalar- indicators to correlate to the shape of the struts.

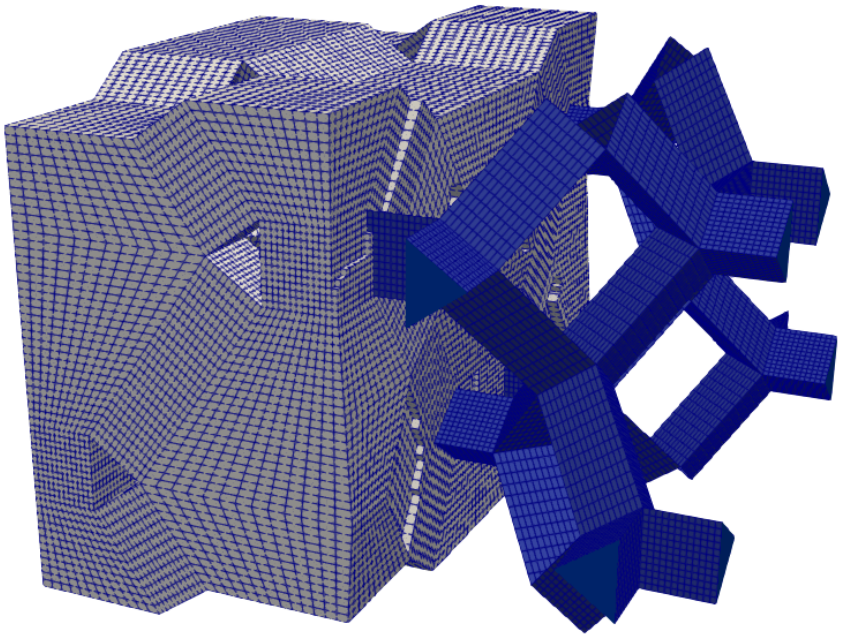

Fig. 2: Left-half computational fluid domain, right-half solid-fluid interface. Porosity: $\varepsilon = 92.5\%$, mesh composed of 290'000 hexahedral elements.

3.1 Coefficient identification for macroscopic laws

Identifying flow properties in porous media is critical for distinguishing regime transitions, if any. As highlighted in the introduction, there are several methods to identify them. We have chosen the one that makes the best use of the our numerical tools. We have chosen the following form of the Forchheimer's equation:

$$-\frac{\Delta p}{L} = \mu K_D^{-1} u + \beta \rho u^2, \tag{4}$$

with β the inertial coefficient (m^{-1}) and ρ is the fluid density ($\mathrm{Kg.m}^{-3}$). The identification method we have used is as follows. First, we use the computed steady-state solutions in the range of very small Reynolds numbers ($Re \in [10^{-5}, 1]$) to identify the Darcian permeability K_D from eq. 4 in which we drop the inertial term (see Figure 4a for the case of porosity $\varepsilon = 0.68$). There are at least seven computations in this range that enable us to perform a highly accurate identification of the K_D coefficient (regression coefficient: 0.9999534). By doing so, we take advantage of the FE method that is particularly efficient for elliptic problems. In a second step, we take the deviation from the Darcy's law as follows:

$$(-\Delta p/L)/u - K_D\ u.$$

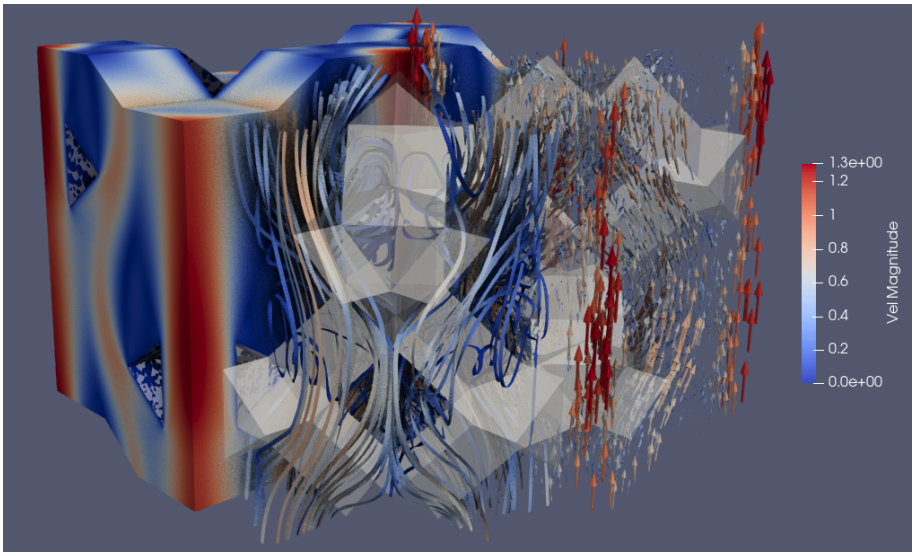

Fig. 3: Computed results at $\mathrm{Re}_{Dh} = 183.7$ for porosity $\varepsilon = 86.4\%$. Ribbons (streamlines of the flow) and velocity vectors (both colorized by velocity magnitude).

This quantity is a linear function of u^2, according to eq. 4. We plot this quantity and perform the linear fit with results from higher values in velocity. From this fit, we can group the pair $(u, \partial < p > /\partial x)$ until the deviation to the linear fit does influence the regression coefficient. We have shown the case of porosity $\varepsilon = 0.68$ in Figure 4b. We have at least 50 continuation points in this range and get regression coefficient of 0.9999. Finally, we extract the inertia coefficient β, which is the slope of this linear fit.

Regarding the case of open-cell foams as the one considered in this work, one has to select one among the various characteristic length scales L_c (m), to build up dimensionless quantities, such as:

- The Reynlods number:

$$Re = \frac{\rho u L_c}{\mu}. \tag{5}$$

- The Darcy friction coefficient:

$$f_D = \frac{\Delta P}{L_c} \frac{2L_c}{\rho u^2}. \tag{6}$$

There is no consensus in the literature for the relevant choice of L_c. The hydraulic diameter, a 3D extension to the cylinder diameter historically used in fluid studies, defined as $D_h = 4\mathrm{V}_f/S_p$, with V_f the volume of the fluid phase (m^3, called the total wetted volume), and S_p the total wetted surface area (m^2) are commonly used.

Other reference quantities are also found in the literature, as the strut length L_s, the periodic length of one cell foam L_p, $\sqrt{K_D}$ only for Darcian flows, or βK_D for

Forchheimer's ones, etc (e.g. [47, 48]), reported in table 1. The first three (D_h, L_p, L_s) are purely geometrical defined quantities. D_h and L_p are macroscopic quantities whereas L_s is a 10 times smaller quantity than the two previous ones. Finally the fourth one, $\sqrt{K_D}$ combines geometrical quantity (porosity, ...) and macroscopic integration of the pressure drop over the cell.

Table 1: Permeabilities, inertia coefficients with length scales for a Kelvin cell of various porosities ε.

	Macroscopic properties		Length scales			
Porosity (%)	K_D (m^2)	β (m^{-1})	D_h (m)	L_p (m)	L_s (m)	$\sqrt{K_D}$ (m)
97.6	0.1190	0.1441	5.17	2.54	0.1	0.3444
92.5	0.0838	0.5989	3.18	2.77	0.2	0.2895
86.4	0.0646	0.9974	2.52	3.00	0.3	0.2542
80.1	0.0519	1.3677	2.19	3.23	0.4	0.2278
68.3	0.0353	2.2202	1.86	3.69	0.6	0.1878

However, it's possible to compare the permeability obtained from previous work with comparable Kelvin cells, since it varies proportionally to the square of the cell size (i.e., $K_D \propto {d_{cell}}^2$). Previous results were obtained with different numerical tools such as Starccm+ (commercial software) and a in-house code using a kinetic method, close to Lattice Boltzmann ([18]). The values computed in the present work (Kelvin cell with triangular struts, numerical model described in §2) are reported in Table 1 and also reported in Figure 5. There is a very good agreement between all methods, whatever being the strut shape.

3.2 Flow regime transitions

Using the dimensionless pressure drop in the form of friction coefficient as a function of the Reynolds number leads to the Moody's diagram. It's the usual way to qualitatively identify transition regimes. Using Fig. 8, we recover three regimes: i) the Darcian one in the linear part with the minus one slope; ii) a first transition departing from the previous linear zone and corresponding to the weak inertia zone; iii) the strong inertia zone. The curves are ordered from top to bottom for increasing porosity ($68.3\% < \varepsilon < 97.6\%$). Indeed, at a given Reynolds number, the friction coefficient increases as the porosity decreases (as it is proportional to the specific surface area).

When increasing the Reynolds number above the Darcian region (of minus one slope in Fig. 8), the departure from the Darcy's law grows as Re increases. So, one computes the distance to the Darcy's law and defines a user defined threshold to identify the critical Reynolds number at which the flow gets out from the Darcian regime. The pressure-drop relationship to the filtration velocity is nearly linear in this zone, and changing this threshold only shifts the critical Reynolds number. For example, taking 1% over 2.5% changes the critical Reynolds of about 25%. In this

work, we have chosen this threshold to be at 2.5%. Fitting the values reported in Table 2, one finds that the Reynolds number evolves as a function of the compacity (1-ε) according to the power law:

$$\mathrm{Re}_{\mathrm{Dh}} = 13.35(1-\varepsilon)^{0.456}. \tag{7}$$

Moving to the transition between weak and strong inertia regions, another method has been used. We represent the flow as the deviation to Darcy's law as a function of u^2 (see Fig. 9). This curve has the weak and strong zones. For simplicity, we can model their respective evolution by a polynomial, for each zone. We found that there is a unique intersection point of those polynomials, representing the point where the transition occurs. With this method, we do not need to define a threshold. The critical Reynolds number related to that transition follow another power law, as follows:

$$\mathrm{Re}_{\mathrm{Dh}} = 2154.4(1-\varepsilon)^{-0.823}. \tag{8}$$

We have compared the values of transitional critical Reynolds number based on different length scales, in Table 2 and 3, summarised in Figure 6. Obviously, the slope's curves depend of the variation of the considered reference length scale. The zone defining the weak inertia flow zone is always of two orders of magnitude in Reynolds number, but is shifted from 0.01 for the strut size considered as the length scale, to 10 for the hydraulic diameter. The shift is so huge that the critical Reynolds transition from weak to strong inertia based on the strut size is at the same order of magnitude of the end of the Darcian regime based on the periodic length.

We can make a mechanical analysis to chose a particular length scale as the characteristic one. Two factors play a high role in modifying the pressure drop: the change of cross section, and the change of direction due to the path taken by the fluid in the porous media. The first one is related to the divergence free velocity field, changing the flow velocity between each section that the fluid cross. The second one is related to the tortuosity of the porous media. Thus, the friction length is related to both parameter. From all the possible length scales cited above, the hydraulic diameter could be seen as a friction length, and therefore could be more accurate to express the changes at which the macroscopic regimes occur. We use from now on the hydraulic diameter as the characteristic length scale.

Table 2: Reynolds number of the right bound of the Darcian validity domain, based on several length scales.

		Re_c (Darcy) based on			
porosity (%)	Compacity (%)	D_h	L_p	L_s	$\sqrt{K_D}$
97.6	2.4	8.59	4.21	0.17	0.57
92.5	7.5	5.61	4.88	0.35	0.51
86.4	13.6	4.22	5.02	0.50	0.43
80.1	19.9	3.45	5.10	0.63	0.36
68.3	31.7	2.61	5.19	0.84	0.26

Table 3: Critical Reynolds number of the transition from weak to strong inertia regimes, based on several length scales.

		Re_c (strong inertia) based on			
porosity (%)	Compacity (%)	D_h	L_p	L_s	$\sqrt{K_D}$
97.6	2.4	1099.2	539.3	21.2	73.2
92.5	7.5	467.0	406.2	29.3	42.4
86.4	13.6	228.8	272.2	27.2	23.1
80.1	19.9	184.4	272.1	33.7	19.2
68.3	31.7	135.4	269.1	43.7	13.7

3.3 Pore-scale analysis: fluid flow bifurcations

Using the numerical tools presented in Section 2, two types of bifurcations have been encountered while spanning the fluid-flow rate in the range of $\mathrm{Re}_{Dh} \in [0 - 2500]$. The first one is the Hopf bifurcation (or dynamic one), and the second one is the steady-state bifurcation (or static one).

We have performed a spatial convergence study (see Table 4) to check the mesh sensitivity on the critical Reynolds number associated with the first encountered bifurcation. We have used a smaller (quarter) representative domain, which enables to get a finer mesh. One effectively gets a convergence to the same critical Reynolds as the mesh gets finer. Applying the LSA to all steady-state solutions computed by the ANM, we find the critical Reynolds numbers associated with the first Hopf bifurcations, reported in Table 5. A steady-state bifurcation study has been done for various porosities and is summarized in Table 6 and Figure 7. The higher the porosity the higher is the Reynolds number for a given pressure drop. For such high porosities the first encountered bifurcation is a Hopf one. This means that the steady-state flow looses at that point its stability towards a periodical limit cycle, telling us that inertia changes the dynamics of the system. On the other hand, for low porosity cases, the Reynolds number is much lower for the same given pressure drop and the first encountered bifurcation is a steady-state one, whose nature is reported in table 6.

The Reynolds numbers associated with such steady-state bifurcations evolve as a function of the porosity according to the following power law:

$$\mathrm{Re}_{\mathrm{Dh}} = 4778.4(1 - \varepsilon)^{-1.03} \tag{9}$$

Two main points are noteworthy. The first one is that in the range of spanned flow rates we found two Hopf bifurcations for the Kelvin foam at porosity 86.4%. It's not uncommon, but we only have this behavior for this porosity. The second remark is that in the range of spanned flow rates we didn't find any Hopf bifurcation for the porosity of 80.1%. In this case, the main branch along the control parameter's path computed by the ANM is unstable. We were able to take the first branch at the steady-state bifurcation point, which is a pitchfork, and take the stable branch. But this bifurcation act like a strong attractor, making it difficult to explore this branch, as this would need further algorithmic developments.

Table 4: Spatial convergence study for the critical Reynolds number Re_c (based on the hydraulic diameter) associated with the first Hopf bifurcation. h is the mean edge size of all the elements of the domain.

porosity = 97.6%	mesh #1	mesh #2	mesh #3	mesh #4
mean h	0.0601	0.0451	0.0361	0.0285
Number of dof	262 466	611 750	1 182 650	2 382 666
Re_c Hopf	1376	1390	1399	1410
Relative error	2.41%	1.38%	0.76%	-

Moreover, from a more practical point of view, the ANM algorithm may sometimes detect some strange bifurcations, specially at low Reynolds number. To check the physical or spurious origin of the computed bifurcations, the kernel size of the algebraic system was also computed. Indeed, at a bifurcation point, the matrix associated to this algebraic problem is rank-deficient. That means that there is different orders in magnitude between the smallest eigenvalues, some at zero to the numeric precision. For each bifurcation candidate, we have checked this property, and we are thus aware of the physical relevance of the steady-state bifurcation. The spurious bifurcations arise when the truncation order of the power series computed by the ANM is too high compared to the spatial discretization. In this case, the errors coming from the spatial discretization grow as the terms of the series expansion get smaller. The bifurcation detection is perturbed by this artefact.

Table 5: Critical Reynolds number associated with the first Hopf bifurcation.

porosity (%)	Re_c Hopf
97.6	710.7
92.5	294.1
86.4	317.5
80.1	-
68.3	154.0

3.4 Discussion: pore-scale instabilities and impact on flow law at macroscopic-scale

After identifying the transition between the various flow regimes (creeping, weak and strong intertia), and found the critical Reynolds numbers associated with the encountered bifurcations (Hopf or steady-state), we can compare their respective position in a same plot (Fig. 10). The first comment is that all bifurcations are located in the vicinity of the transition between the weak and strong inertia regimes. They occur at moderate Reynolds numbers that depend on the foam porosity, (expressed in term

.

Table 6: Critical Reynolds associated with the first steady-state bifurcation, with the bifurcation type

porosity (%)	Re_c for steady-state bifurcation	bifurcation type
97.6	2077.5	transcritical
92.5	485.6	pitchfork
86.4	385.7	pitchfork
80.1	209.7	pitchfork
68.3	137.6	transcritical

of compacity). The Hopf bifurcations are mainly located just before this transition, whereas the steady-state ones are located just beyond it. Moreover, as the porosity decreases, the steady-state bifurcations occur much closer to the transition between the weak and strong inertia regimes.

Both steady-state and Hopf bifurcations have at least one eigenvalue that has a null real part. The hopf bifurcation has a non null imaginary part, whereas the steady-state one is null. They both indicate a stability change, where any non-infinitesimal perturbation results in a change in the fluid-flow pattern or feature. It thus makes sense to gather them and represent their evolution using the same fitting curve, which has been shown in Fig. 10 (solid black line). This curve is almost confounded with the transition from weak to strong inertia regimes, which has been clearly established. The bifurcations which are fluid-flow instabilities at pore-scale, are then located in the area where the inertia terms are more significant as compared to the viscous forces. They happen at a relatively moderate Reynolds number and clearly depend on the porosity. No more detailed influence of foam geometry (e.g. strut shape) has yet been obtained.

4 Conclusion

The incompressible Navier-Stokes equations have been computed at the pore-scale in a Kelvin foam in order to get all knowledge necessary to identify a macroscopic behavior in such periodic geometry. We have identified macroscopic properties such as the permeability and the inertia term of a complex idealized 3D foams. To do so, we considered the first order polynomial of the Forchheimer's equation to be the Darcian permeability and identified in a subsequent step the inertia term.

We have introduced a systematic way to define flow transitions from three different regimes (creeping, weak and strong inertia), in which the flow has different macroscopic behaviors. They all follow a power law equation, whose fitting parameters have been given.

To our knowledge, it's the first time that the ANM and LSA method were used to automatically detect bifurcations in such complex geometrical fluid-flow configurations. We found some steady-state and Hopf bifurcations, for Kelvin cells with various porosities. We have correlated the critical Reynolds numbers related to those bifurcations to the flow regimes and showed that they appear in the vicinity of the transition from weak to strong inertia regimes. This strong result validates our methodology in defining flow transitions, where flow behavior changes. We may also emphasize that

the used numerical strategies are computationally efficient, as they rely on steady-state solutions to perform linear stability analyses.

We partially used the field information given by the direct numerical solutions in such spatially resolved configurations. Some other valuable quantities can be exploited in a future work, such that the eigenvector field associated with the most unstable mode given by the LSA, which provides the most dangerous perturbation field along with its magnitude. It will help to better understand the flow behavior, linking it to the foam geometry.

Acknowledgments. Centre de Calcul Intensif d'Aix-Marseille is acknowledged for granting access to its high performance computing resources.

References

[1] Darcy, H.: Les fontaines publiques de la ville de dijon. Victor Dalmont, Paris (1856)

[2] Forchheimer, P.H.: Wasserbewegung durch boden. z. vereines dtsch. Ing **45**, 1792–1788 (1901)

[3] Kumar, P., Topin, F.: State-of-the-Art of Pressure Drop in Open-Cell Porous Foams: Review of Experiments and Correlations. Journal of Fluids Engineering **139**(11), 111401 (2017) https://doi.org/10.1115/1.4037034 https://asmedigitalcollection.asme.org/fluidsengineering/article-pdf/139/11/111401/6201838/fe_139_11_111401.pdf

[4] Kumar, P., Topin, F.: Predicting pressure drop in open-cell foams by adopting forchheimer number. International Journal of Multiphase Flow **94**, 123–136 (2017) https://doi.org/10.1016/j.ijmultiphaseflow.2017.04.010

[5] Kumar, P., Topin, F.: Investigation of fluid flow properties in open cell foams: Darcy and weak inertia regimes. Chemical Engineering Science **116**, 793–805 (2014) https://doi.org/10.1016/j.ces.2014.06.009

[6] Kumar, P., Topin, F.: Micro-structural impact of different strut shapes and porosity on hydraulic properties of kelvin-like metal foams. Transport in Porous Media **105**, 57–81 (2014) https://doi.org/10.1007/s11242-014-0358-8

[7] Firdaouss, M., Guermond, J.-L., Le Quéré, P.: Nonlinear corrections to darcy's law at low reynolds numbers. Journal of Fluid Mechanics **343**, 331–350 (1997) https://doi.org/10.1017/S0022112097005843

[8] Muskat, M.: The flow of homogeneous fluids through porous media. The Mapple Press Company, York, PA **25**, 58–67 (1946)

[9] Mei, C.C., Auriault, J.-L.: The effect of weak inertia on flow through a porous medium. Journal of Fluid Mechanics **222**, 647–663 (1991)

[10] Pauthenet, M., Davit, Y., Quintard, M., Bottaro, A.: Inertial sensitivity of porous microstructures. Transport in Porous Media **125**, 211–238 (2018) https://doi.org/10.1007/s11242-018-1115-1

[11] Ward, J.C.: Turbulent flow in porous media. Journal of the Hydraulics Division **90**(5), 1–12 (1964) https://doi.org/10.1061/JYCEAJ.0001096 https://ascelibrary.org/doi/pdf/10.1061/JYCEAJ.0001096

[12] Azzam, M.I.S., Dullien, A.L.: Flow rate-pressure gradient measurements in periodically nonuniform capillary tubes. AIChEJ **19**, 22–229 (1973)

[13] Ruth, D., Ma, H.: On the derivation of the forchheimer equation by means of the averaging theorem. Transport in Porous Media **7**, 255–264 (1992) https://doi.org/10.1007/BF01063962

[14] Giorgi, T.: Derivation of the forchheimer law via matched asymptotic expansions. Transport in Porous Media **29**, 191–206 (1997) https://doi.org/10.1023/A:1006533931383

[15] Whitaker, S.: The forchheimer equation: A theoretical development. Transport in Porous Media **25**, 27–61 (1996) https://doi.org/10.1007/BF00141261

[16] Yazdchi, K., Luding, S.: Towards unified drag laws for inertial flow through fibrous materials. Chemical Engineering Journal **207-208**, 35–48 (2012) https://doi.org/10.1016/j.cej.2012.06.140 . 22nd International Symposium on Chemical Reaction Engineering (ISCRE 22)

[17] Narváez, A., Yazdchi, K., Luding, S., Harting, J.: From creeping to inertial flow in porous media: a lattice boltzmann–finite element study. Journal of Statistical Mechanics: Theory and Experiment **2013**(02), 02038 (2013) https://doi.org/10.1088/1742-5468/2013/02/P02038

[18] Jobic, Y., Kumar, P., Topin, F., Occelli, R.: Determining permeability tensors of porous media: A novel 'vector kinetic' numerical approach. International Journal of Multiphase Flow **110**, 198–217 (2019) https://doi.org/10.1016/j.ijmultiphaseflow.2018.09.007

[19] Jobic, Y., Kumar, P., Topin, F., Occelli, R.: Transport properties of solid foams having circular strut cross section using pore scale numerical simulations. Heat and Mass Transfer **54**(08), 2351–2370 (2018) https://doi.org/10.1007/s00231-017-2193-2

[20] Ergun, S.: Fluid flow through packed columns. Chemical Engineering Progress **48**, 89–94 (1952)

[21] Kumar, P., Topin, F.: State-of-the-Art of Pressure Drop in Open-Cell Porous Foams: Review of Experiments and Correlations. Journal of Fluids Engineering

139(11) (2017) https://doi.org/10.1115/1.4037034

[22] Ryland, D.K., Nandakumar, K.: A bifurcation study of convective heat transfer in porous media. Part II: Effect of tilt on stationary and non-stationary solutions*. Physics of Fluids A: Fluid Dynamics **4**(9), 1945–1958 (1992) https://doi.org/10.1063/1.858364 https://pubs.aip.org/aip/pof/article-pdf/4/9/1945/12640040/1945_1_online.pdf

[23] Riley, D.S., Winters, D.K.H.: Time-periodic convection in porous media: the evolution of hopf bifurcations with aspect ratio. Journal of Fluid Mechanics **223**, 457–474 (1991) https://doi.org/10.1017/S0022112091001490

[24] Weinitschke, H.J., Nandakumar, K., Ravi Sankar, S.: A bifurcation study of convective heat transfer in porous media. Physics of Fluids A: Fluid Dynamics **2**(6), 912–921 (1990) https://doi.org/10.1063/1.857817 https://pubs.aip.org/aip/pof/article-pdf/2/6/912/12772823/912_1_online.pdf

[25] Samanta, A.: Linear stability of a plane couette–poiseuille flow overlying a porous layer. International Journal of Multiphase Flow **123**, 103160 (2020) https://doi.org/10.1016/j.ijmultiphaseflow.2019.103160

[26] Liu, R., Liu, Q.: Instabilities of a liquid film flowing down an inclined porous plane. Phys. Rev. E **80**, 036316 (2009) https://doi.org/10.1103/PhysRevE.80.036316

[27] Sengupta, S., De, S.: Stability of poiseuille flow of a bingham fluid overlying an anisotropic and inhomogeneous porous layer. Journal of Fluid Mechanics **874**, 573–605 (2019) https://doi.org/10.1017/jfm.2019.464

[28] Agnaou, M., Lasseux, D., Ahmadi, A.: From steady to unsteady laminar flow in model porous structures: an investigation of the first hopf bifurcation. Computers and Fluids **136**, 67–82 (2016) https://doi.org/10.1016/j.compfluid.2016.05.030

[29] Deng, N., Pastur, L.R., Tuckerman, L.S., Noack, B.R.: Coinciding local bifurcations in the navier-stokes equations. Europhysics Letters **135**(2), 24002 (2021) https://doi.org/10.1209/0295-5075/ac182a

[30] Dhatt, G., Touzot, G., Lefrançois, E.: Methode des éléments finis - une présentation (2004)

[31] Carey, G.F., Krishnan, R.: Penalty finite element method for the navier-stokes equations. Computer Methods in Applied Mechanics and Engineering **42**(2), 183–224 (1984) https://doi.org/10.1016/0045-7825(84)90025-2

[32] Cochelin, B., Medale, M.: Power series analysis as a major breakthrough to improve the efficiency of asymptotic numerical method in the vicinity of bifurcations. Journal of Computational Physics **236**, 594–607 (2013) https://doi.org/10.1016/j.jcp.2012.11.016

[33] Medale, M., Cochelin, B.: High performance computations of steady-state bifurcations in 3d incompressible fluid flows by asymptotic numerical method. Journal of Computational Physics **299**, 581–596 (2015) https://doi.org/10.1016/j.jcp.2015.07.021

[34] Nicolis, G.: Introduction to Nonlinear Science. Cambridge University Press, ??? (1995). https://doi.org/10.1017/CBO9781139170802

[35] Medale, M., Cochelin, B., Bissen, E., Alpy, N.: A one-dimensional full-range two-phase model to efficiently compute bifurcation diagrams in sub-cooled boiling flows in vertical heated tube. Journal of Computational Physics **404**, 109131 (2020) https://doi.org/10.1016/j.jcp.2019.109131

[36] Guermond, J.L., Shen, J.: A new class of truly consistent splitting schemes for incompressible flows. Journal of Computational Physics **192**(1), 262–276 (2003) https://doi.org/10.1016/j.jcp.2003.07.009

[37] Cochelin, B., Damil, N., Potier-Ferry, M.: Méthode asymptotique numérique. Hermès - Lavoisier (2007)

[38] Amestoy, P.R., Duff, I.S., Koster, J., L'Excellent, J.-Y.: A fully asynchronous multifrontal solver using distributed dynamic scheduling. SIAM Journal on Matrix Analysis and Applications **23**(1), 15–41 (2001)

[39] Amestoy, P.R., Buttari, A., L'Excellent, J.-Y., Mary, T.: Performance and Scalability of the Block Low-Rank Multifrontal Factorization on Multicore Architectures. ACM Transactions on Mathematical Software **45**, 2–1226 (2019)

[40] Balay, S., Abhyankar, S., Adams, M.F., Brown, J., Brune, P., Buschelman, K., Dalcin, L., Dener, A., Eijkhout, V., Gropp, W.D., Kaushik, D., Knepley, M.G., May, D.A., McInnes, L.C., Mills, R.T., Munson, T., Rupp, K., Sanan, P., Smith, B.F., Zampini, S., Zhang, H., Zhang, H.: PETSc users manual. Technical Report ANL-95/11 - Revision 3.13, Argonne National Laboratory (2020)

[41] Balay, S., Gropp, W.D., McInnes, L.C., Smith, B.F.: Efficient management of parallelism in object oriented numerical software libraries. In: Arge, E., Bruaset, A.M., Langtangen, H.P. (eds.) Modern Software Tools in Scientific Computing, pp. 163–202. Birkhauser Press, ??? (1997)

[42] Balay, S., Abhyankar, S., Adams, M.F., Brown, J., Brune, P., Buschelman, K., Dalcin, L., Dener, A., Eijkhout, V., Gropp, W.D., Kaushik, D., Knepley, M.G., May, D.A., McInnes, L.C., Mills, R.T., Munson, T., Rupp, K., Sanan, P., Smith, B.F., Zampini, S., Zhang, H., Zhang, H.: PETSc Web page. https://www.mcs.anl.gov/petsc (2020)

[43] Hernandez, V., Roman, J.E., Vidal, V.: SLEPc: A scalable and flexible toolkit for the solution of eigenvalue problems. ACM Trans. Math. Software **31**(3), 351–362

(2005)

[44] Kumar, P., Topin, F.: The geometric and thermohydraulic characterization of ceramic foams: An analytical approach. Acta Materialia **75**, 273–286 (2014) https://doi.org/10.1016/j.actamat.2014.04.061

[45] Klostermann, J., Schwarze, R., Brücker, C.: Meshing of porous foam structures on the micro-scale. Engineering with Computers **29**(1), 95–110 (2013) https://doi.org/10.1007/s00366-011-0247-5

[46] Kanaun, S., Tkachenko, O.: Effective conductive properties of open-cell foams. International Journal of Engineering Science **46**(6), 551–571 (2008) https://doi.org/10.1016/j.ijengsci.2008.01.012 . Special Issue: Micromechanics of Materials

[47] Zami-Pierre, F., Loubens, R., Quintard, M., Davit, Y.: Transition in the flow of power-law fluids through isotropic porous media. Phys. Rev. Lett. **117**, 074502 (2016) https://doi.org/10.1103/PhysRevLett.117.074502

[48] Mills, N.J.: The wet kelvin model for air flow through open-cell polyurethane foams. Journal of Materials Science **40**, 5845–5851 (2005)

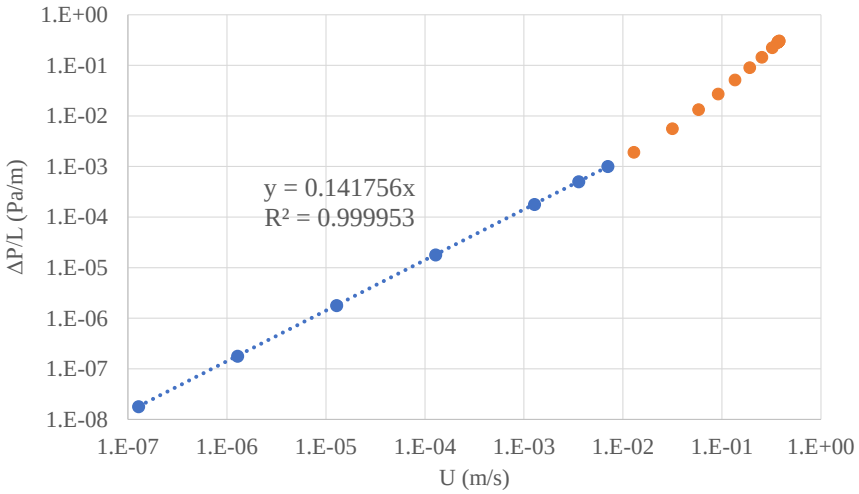

(a) Determination of the permeability K_D.

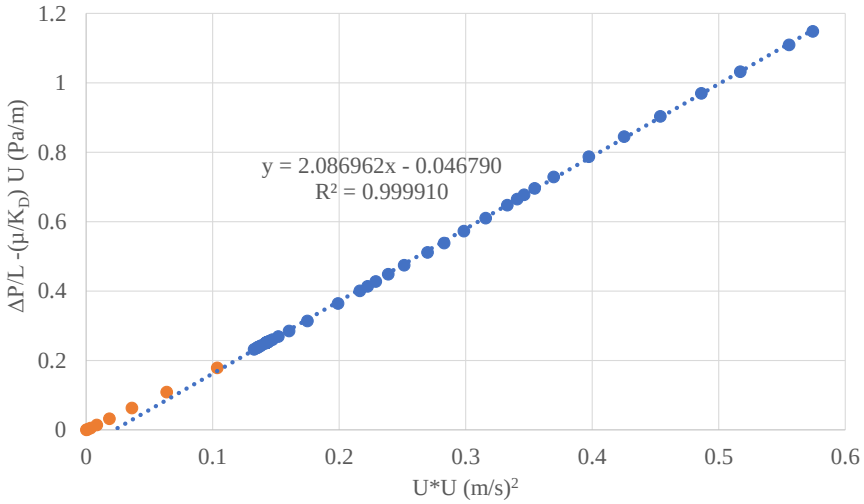

(b) Determination of the inertia coefficient β.

Fig. 4: Identification of the macroscopic flow properties of a Kelvin cell for the porosity $\varepsilon = 0.68$.

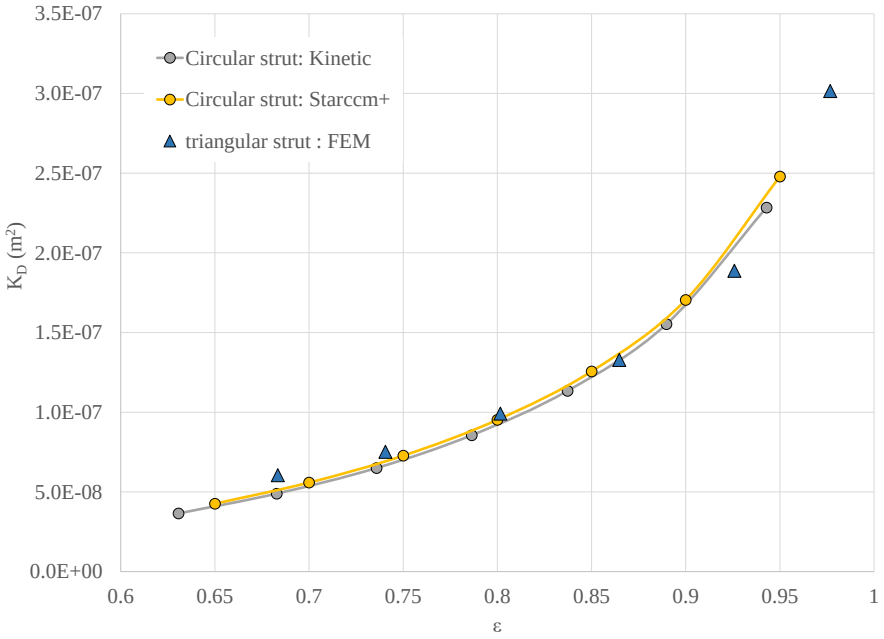

Fig. 5: Comparison of permeability in various Kelvin foams (computed with different numerical methods) [18].

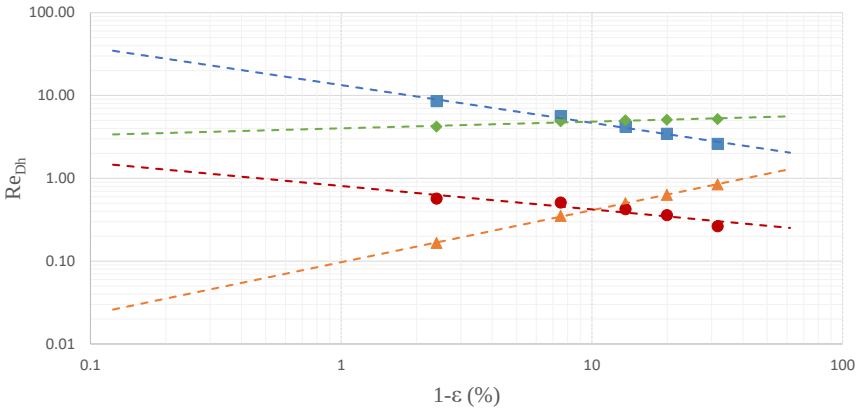

(a) Critical Reynolds number for the transition from Darcy to weak inertia regimes.

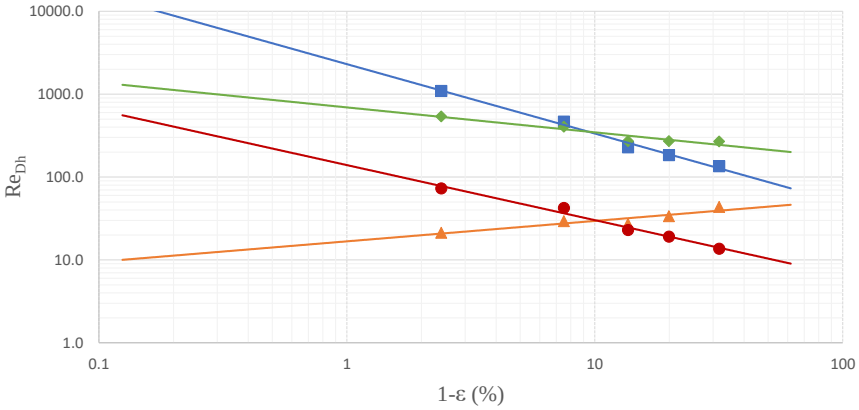

(b) Critical Reynolds number for the transition from weak to strong inertia regimes.

Fig. 6: Critical Reynolds number for the transition from Darcy to weak inertia regimes (dotted lines) and for the weak to strong inertia regimes (solid lines). The square marks refer to the length scale based on the hydraulic diameter, the diamond marks for the periodic length, the triangular marks for the strut size and the circle marks for $\sqrt{\mathrm{K}_D}$.

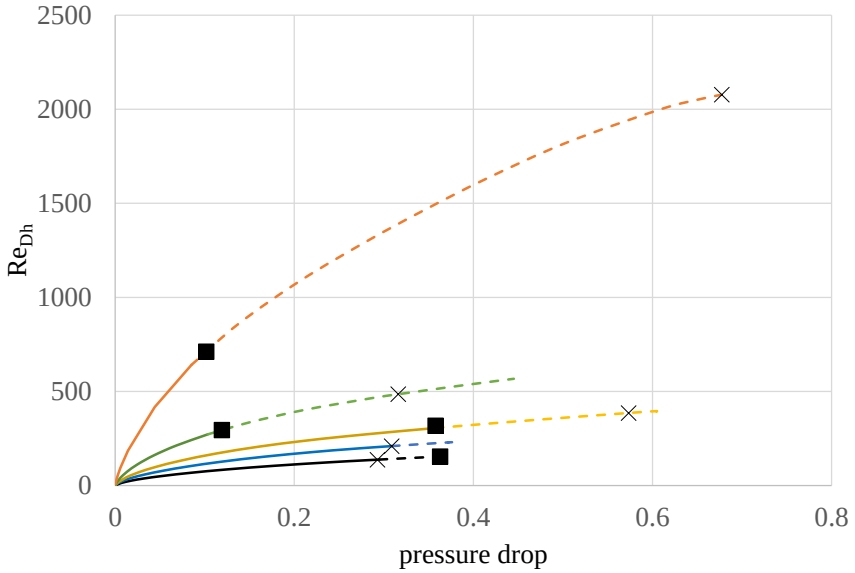

Fig. 7: Bifurcation diagram for various porosities in a Kelvin cell. The solid lines represent stable steady-states, dash line represent instable ones; bold squares represent Hopf bifurcation point, and crosses steady-state bifurcation ones. Orange: $\varepsilon = 0.97$, green: $\varepsilon = 0.92$, yellow: $\varepsilon = 0.86$, blue: $\varepsilon = 0.80$, black: $\varepsilon = 0.68$.

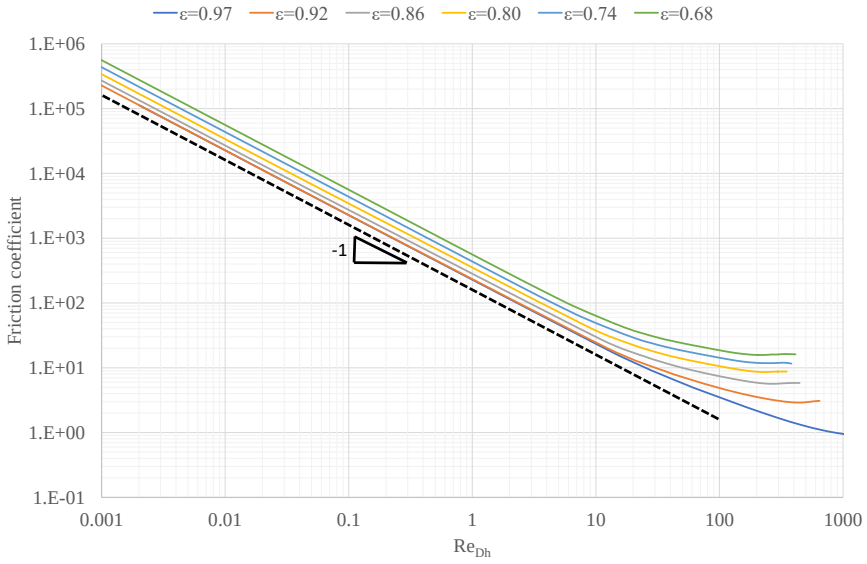

Fig. 8: Moody's diagram.

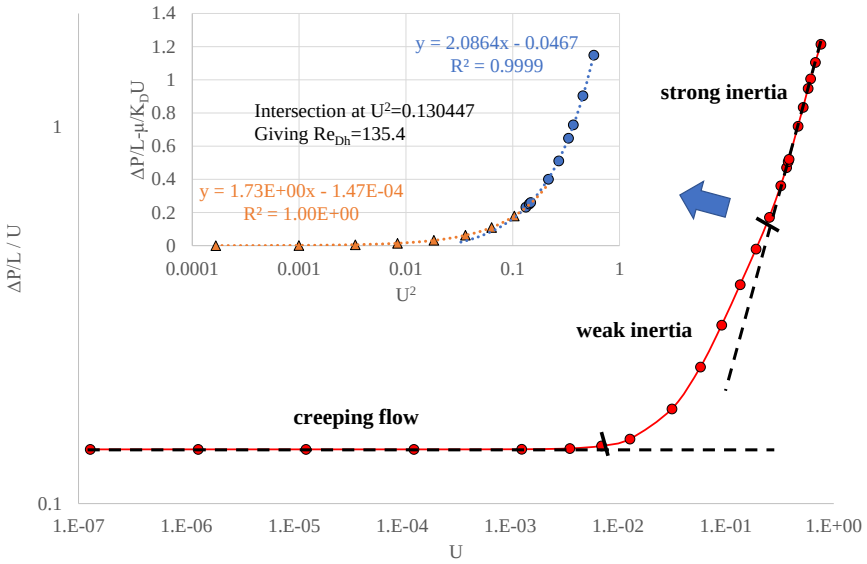

Fig. 9: Quantitative determination of flow regime's transitions.

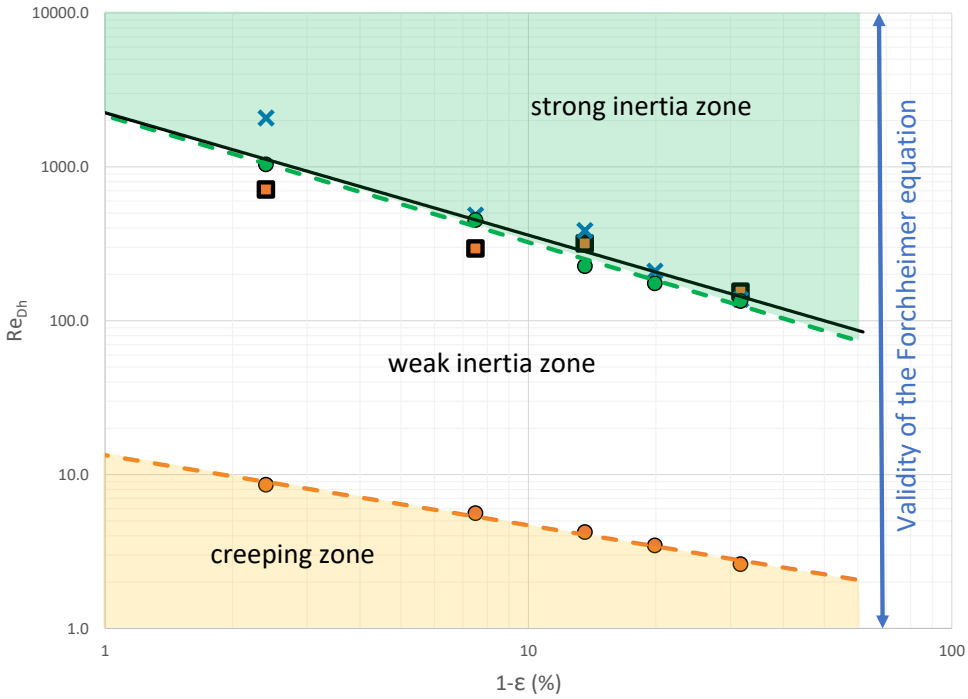

Fig. 10: Validity domain of macroscopic laws along with the critical Reynolds numbers associated with the computed bifurcations. Transition between regimes are represented by dashed lines. Steady-state bifurcations are represented by a cross, Hopf bifurcations by a squares. The fit of all bifurcations is represented by a black line.